Solving an IBEM with Supporting Vector Analysis to Design Quiet TMS Coils

Clemente Cobos Sánchez[a], Francisco Javier Garcia-Pacheco[b], Jose Maria Guerrero-Rodriguez[a], Luis Garcia-Barrachina[c]

[a]*Depto. Ingeniería de Sistemas y Electrónics, Avenida de la Universidad, 10, E-11519, Puerto Real (Cádiz), Spain*
[b]*Depto. de Matemáticas, Universidad de Cádiz, Spain*
[c]*Depto. Ingeniería de Mecánica y Diseño Industrial, Universidad de Cádiz, Spain*

Abstract

Transcranial magnetic stimulation is a promising tool in neuroscience of which successful development is affected by the loud click noise originated when the stimulating coil is energized. This undesired sound is produced by the coil winding deformations generated by the Lorentz self-forces in the TMS device. Addressing the need for TMS systems that produce less noise, a quiet coil design technique is proposed in this work, where instead of minimizing directly the coil deflection, the Lorentz self-force is optimized in order to reduce the acoustic noise. The presented method is based on a stream function IBEM for TMS coil design in which new computational models have been incorporated into the optimization problem, which is efficiently solved by using supporting vector analysis. Several examples of coils of different geometries were designed and simulated to demonstrate the efficiency of the suggested IBEM approach to produce TMS devices that experience minimum Lorentz self-forces. In order to evaluate the acoustic response of the designed TMS coils, the commercial MSC/NASTRAN was used to find the coil deflection. The obtained results show that significant noise reduction can be achieved by minimizing the Lorentz self-force over the TMS coil surface.

Keywords: IBEM, coil design, TMS, Lorentz force.

Email address: clemente.cobos@uca.es (Clemente Cobos Sánchez)

1. Introduction

Transcranial Magnetic Stimulation (TMS) is a non-invasive technique to stimulate the brain, which is applied to studies of cortical effective connectivity, presurgical mapping, psychiatric and medical conditions, such as major depressive disorder, schizophrenia, bipolar depression, post-traumatic, stress disorder and obsessive-compulsive disorder, amongst others [1]. In TMS, strong, brief current pulses driven through a coil are used to induce an electric field stimulating neurons in the cortex. The TMS stimulator most commonly employed is the so called round or figure-of-eight or butterfly coil, although over the last years numerous TMS coil designs have been proposed to improve the coil performance and spatial characteristics of the electromagnetic stimulation [2].

The high coil currents employed in TMS (typical peak values are in the range of several kiloamperes) can generate large magnetic fields (of the order of a few teslas [1]) capable of producing considerable internal forces in the coil. As a consequence, during normal TMS procedure, each current pulse can be accompanied by a clicking noise originated from the internal deflections of the coil windings due to current coil interacting with its own magnetic field, that is, the produced time varying Lorentz force distribution results in vibration of the TMS coil that generates the unwanted click sound.
The levels of noise generated by the Lorentz self-forces can be higher than 120 dB of sound pressure level, which exceed the recommended auditory safety limits [3], becoming then a notable safety problem. In TMS patients, the undesired sound can activate the auditory cortex, affecting so the interpretation of the psychological effects caused by TMS and degrading the focality of the stimulation. Furthermore, the unwanted auditory click can have some others ancillary effects, such as, the propagation of the mechanical vibration through the skull to the cochlea, which can increase the noise sensation. Likewise, such impulsive noise can potentially cause acoustic trauma [4], especially in repetitive TMS operators.
This safety concern in TMS has been traditionally addressed as an afterthought, which have been partially mitigated with technical solutions such as hearing protection to attenuate the sound or usage of absorbent materials in the coil structure for acoustic dissipation. Furthermore, at the present the literature relevant to the TMS noise problem is scarce, and the most notable efforts are based on the control of the current pulse shape in order to reduce the audible frequencies components, and so to mitigate the sound sensation [5]-

[6]. Nonetheless, authors of this work are not aware of any method capable of considering the acoustic noise or vibrations of a coil during the design process, which unquestionably would benefit the development of TMS and its application in cognitive neuroscience.

In general, the problem in TMS coil design is to find optimal positions for the multiple windings of coils so as to produce fields with the desired spatial characteristics and properties (high focality, field penetration depth, low inductance, low heat dissipation, etc.). Amongst all strategies developed over the last years to design TMS coils, there is an especially successful group formed by those techniques that rely on a description of the design problem in terms of the stream function of a quasi-static continuous surface current density. A notable example is the work of Koponen *et al.* [7] who presented method for designing spherical minimum-energy TMS coils with given focality constraints. Cobos Sánchez *et al.* incorporated the stream function within an inverse boundary element method (IBEM) [8] to produce TMS coils with arbitrary geometry subjected to different constraints (such as minimum power dissipation).

Later, a stream function IBEM approach was used to include new coil features in the design process such as maximum current density or reduced temperature [9], in this latter work a novel optimisation framework based on supporting vector analysis was developed to guarantee the optimality of the resulting coil solutions.

More recently, the concept of stream function has kept been used to produce a methodology for designing TMS coils to achieve optimal trade-off between the depth and focality of the induced electric field, as well as the energy required by the coil [10]; and for producing spherical shaped cap coils that can replicate the stimulation of existing TMS coils while reducing energy [11].

In this work, by taking advantage of the versatility of the stream function IBEM, we demonstrate that coils of arbitrary geometry with reduced Lorentz self-forces may be designed, which can be used as an efficient strategy to produce TMS devices that generates less acoustic click noise.

The presented TMS coil design method is based on an existing stream function IBEM approach [9], in which new coil magnitudes, such as the Lorentz self-force, have been prototyped. These novel computational models have been subsequently incorporated into an optimisation framework specially developed with supporting vector analysis for the design of TMS coils of arbitrary shape with optimal Lorentz self-forces.

Furthermore, the study of the noise produced by a coil is frequently achieved

by calculating its deformation [12]. In this work, to evaluate the acoustic noise reduction, the linear static solver provided by the commercialized finite element (FE) software MSC/NASTRAN has been employed for the calculation of the deflection response of the TMS coils presented.

This paper is arranged as follows: firstly a brief outline of the stream function IBEM framework is given, followed by the numerical description of the Lorentz self-force experienced by the coil. The developed computational models are used to pose the TMS coil design as an optimization problem which is suitably reformulated to be solved by using supporting vector analysis. We illustrate the efficacy of the proposed approach with the design and simulation of a set of minimum inductance TMS coils of different geometry with optimal Lorentz self-forces, where the mechanical behaviour of each stimulator is compared with conventional TMS designs. Finally, the commercial software MSC/NASTRAN is used to evaluated the acoustic response of the designed coils.

2. Method

2.1. Theory

Here we begin by reproducing a brief outline of the computational model described in the original work [8]-[9]. In an IBEM for TMS coil design the current density is found through the solution to an optimisation problem, which is formulated in terms of the associated stream function. In order to model such a current distribution the conducting surface of the coil, S, is discretized into T triangular elements with N nodes, which are lying at each vertex of the element. The current density at a given point at the surface can be then written as

$$\mathbf{J}(\mathbf{r}) \approx \sum_{n=1}^{N} \psi_n \, \boldsymbol{\jmath}^n(\mathbf{r}), \qquad \mathbf{r} \in S, \tag{1}$$

where $\psi = [\psi_1, \psi_2, \ldots, \psi_N]^T$ is the vector containing the nodal values of the stream function, which are the optimization variables and $\boldsymbol{\jmath}^n$ is the current element associated to the n^{th}-node.
By using the current density model in equation 1, the discretized expressions for the required physical magnitudes involved in the problem can be obtained. For instance, the magnetic field created by the coil at a given point can be

written as

$$\mathbf{B}(\mathbf{r}) \approx \sum_{n=1}^{N} \psi_n \mathbf{b}^n(\mathbf{r}), \qquad \mathbf{r} \in \mathbb{R}^3, \tag{2}$$

where $\mathbf{b}^n$ is the magnetic induction vector produced by a unit stream function at the *nth*-node [8].
Analogously, the electric field induced by the current density at a given point can be modelled as [15]

$$\mathbf{E}(\mathbf{r}) \approx \sum_{n=1}^{N} \psi_n \mathbf{e}^n(\mathbf{r}), \qquad \mathbf{r} \in \mathbb{R}^3, \tag{3}$$

where $\mathbf{e}^n$ is the E-field induced by a unit stream function at the *nth*-node.

Moreover, calculation of the electric (equation 3) and magnetic (equation 2) fields can be used to get more insight in its mechanical stability. More precisely, a stress analysis of the coil can be achieved by firstly determining the Maxwell stress tensor $T_{i,j}$

$$T_{i,j} = \varepsilon_0 (E_i E_j - \frac{1}{2}\delta_{i,j} E^2) + \frac{1}{\mu_0}(B_i B_j - \frac{1}{2}\delta_{i,j} B^2), \tag{4}$$

and finally by computing the von Mises stress [13], which is given by

$$\sigma_\nu = \sqrt{T_{xx}^2 + T_{yy}^2 + T_{zz}^2 - T_{xx}T_{yy} - T_{xx}T_{zz} - T_{yy}T_{zz} + 3(T_{xy}^2 + T_{xz}^2 + T_{yz}^2)}. \tag{5}$$

2.2. Lorentz self-force

In the following the new computational model of the Lorentz self-force is described, which subsequently will be incorporated into the stream function IBEM so as to study the reduction of the click noise.
Let us first recall that a current density, $\mathbf{J}$, flowing in a magnetic field, $\mathbf{B}$ experiences a Lorentz force density, $\mathbf{f}$, given by

$$\mathbf{f}(\mathbf{r}) = \mathbf{J}(\mathbf{r}) \times \mathbf{B}(\mathbf{r}). \tag{6}$$

By incorporating the numerical expression of the current density, equation 1, and magnetic induction, equation 2, into equation 6 the following model for the Lorentz self-force produced by the current density is obtained

$$\mathbf{f}(\mathbf{r}) \approx \sum_{n,m=1}^{N} \psi_n \psi_m \boldsymbol{\jmath}^n(\mathbf{r}) \times \mathbf{b}^m(\mathbf{r}) = \sum_{n,m=1}^{N} \psi_n \psi_m \mathbf{f}^{n,m}(\mathbf{r}), \qquad \mathbf{r} \in \mathbb{R}^3. \tag{7}$$

where $\mathbf{f}^{n,m} = \boldsymbol{\jmath}^n(\mathbf{r}) \times \mathbf{b}^m(\mathbf{r})$ is related to the Lorentz force density experienced by the current element associate to the n^{th}-node due to the magnetic field created by the m^{th}-node.

2.3. Matrix formulation

The design problems proposed in this work have been tackled using the optimization framework developed in [9], where a TMS coil design is posed as a convex optimisation. To this end, the presented and previously developed numerical models are used to produce matrix equations that transform $\psi \in \mathbb{R}^N$ into the various coil properties (Appendix A), which allows us to formulate the design optimization problem:

- The magnetic stored energy in the coil [8]

$$\psi^T L \psi, \qquad L \in \mathbb{R}^{N \times N}, \tag{8}$$

  where L is the inductance matrix, a full symmetric positive definite matrix.

- The electric field induced in a series of M points inside of a conducting system [14], $\{\mathbf{r}_1, \mathbf{r}_2, \ldots, \mathbf{r}_M\}$

$$\mathcal{E}_j \psi, \qquad \mathcal{E}_j \in \mathbb{R}^{M \times N}, \ j = x, y, z. \tag{9}$$

- The Lorentz self-force density experienced by one mesh element of the conducting surface current due to the coil magnetic field

$$\psi^T \mathcal{F}_{j,t} \psi, \qquad \mathcal{F}_{j,t} \in \mathbb{R}^{N \times N}, \quad t = 1, \ldots, T, \quad j = x, y, z, \tag{10}$$

  where $\mathcal{F}_{j,t}(n,m)$ is the $j-$component of $\boldsymbol{f}^{n,m}$ when evaluated at the barycentre of the t^{th}-element, that is

$$\mathcal{F}_{j,t}(n,m) = f_j^{n,m}(\mathbf{r}_t), \qquad n, m = 1, \ldots N, \qquad t = 1, \ldots, T, \ j = x, y, z. \tag{11}$$

3. Optimization

TMS Coils of rectangular flat, spherical and hemispherical form are considered in this work; for each geometry two minimum inductance TMS coils are produced to stimulate an equivalent region of interest (ROI). The first one is a conventional coil (with no constraints in the Lorentz self-force) used as reference, whereas the second coil is designed to have a reduced acoustic noise by minimizing the Lorentz self-force over its surface.
The reference TMS stimulator for each coil geometry is obtained through the solution of the following optimization problem [9]

$$\begin{cases} \max \|\mathcal{E}_x\psi\|_2^2 + \|\mathcal{E}_y\psi\|_2^2 + \|\mathcal{E}_z\psi\|_2^2 \\ \min \psi^T L\psi. \end{cases} \tag{12}$$

In order to reduce the acoustic noise produced by the reference TMS stimulators, minimization of the Lorentz self-force at each mesh element of the coil surface is considered, which is achieved by including the following $3 \times T$ conditions into equation 12 to yields the following optimization problem

$$\begin{cases} \max \|\mathcal{E}_x\psi\|_2^2 + \|\mathcal{E}_y\psi\|_2^2 + \|\mathcal{E}_z\psi\|_2^2 \\ \min \psi^T \mathcal{F}_{x,t}\psi \qquad t = 1, \ldots, T \\ \min \psi^T \mathcal{F}_{y,t}\psi \qquad t = 1, \ldots, T \\ \min \psi^T \mathcal{F}_{z,t}\psi \qquad t = 1, \ldots, T \\ \min \psi^T L\psi. \end{cases} \tag{13}$$

Appendix B details the reformulation of equation 13 into the following equivalent optimization

$$\begin{cases} \max \|\mathcal{E}_x\psi\|_2^2 + \|\mathcal{E}_y\psi\|_2^2 + \|\mathcal{E}_z\psi\|_2^2 \\ \min \psi^T L\psi \\ \min \|C\psi\|_2^2, \end{cases} \tag{14}$$

where C is a matrix can be constructed by combination of the Cholesky decomposition of each $\mathcal{F}_{j,t}$ $t = 1, \ldots, T$ and $j = x, y, z$. Problem in equation equation 14 can be efficiently solved by employing supporting vector analysis (see Appendix B for more detail).

4. Problems

In this section, examples of TMS coils problems solved by using the proposed stream function IBEM technique are presented. These designs were based on three different coil forms.

4.1. Rectangular Flat Coils

The first geometry considered is that of a rectangular flat form of 14 cm $\times$ 7.5 cm located at the $xy-$plane, which has been meshed with $T = 4800$ elements and $N = 2501$ nodes; and where TMS coils have been designed to have minimum inductance and maximise the magnitude of the electric field induced in a prescribed ROI, which is made up of $M = 400$ points inside a spherical region of radius 1 cm that is centred on the z-axis, and 3 cm below the rectangular conducting surface, as illustrated in figure 1(a).

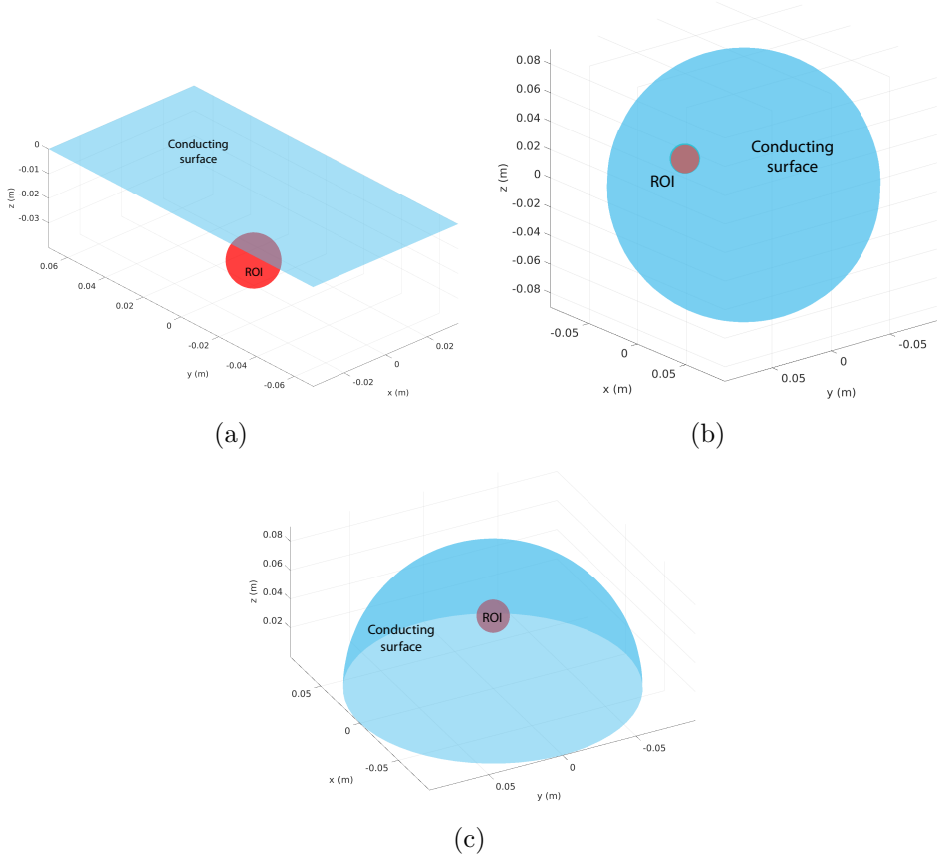

Figure 1: *Schematic diagram showing the conducting surface for a) CoilP0 and CoilP, b) CoilS0 and CoilS and c) CoilH0 and CoilH coil design problems respectively, along with the corresponding region of interest (ROI) in which the desired stimulation must be achieved in each case.*

The reference TMS stimulator for this geometry is referred to as CoilP0,

and it is obtained through the solution of equation 12, whereas CoilP is the stimulator obtained by solving equation 14 in the case of the rectangular coil form and this particular choice of the ROI.

4.2. Spherical coils

TMS coils of spherical geometry have been frequently proposed in the literature [7], [10], [11] as this particular form is well matched to the head. Here we have tackled the design of minimum inductance spherical TMS coils of radius 9 cm, which are designed to induce a maximum E-field in a spherical ROI of 1 cm radius, made up of $M = 400$ points, shifted by 5 cm and 3 cm in the positive $y-$ and $z-$directions respectively from the centre of the conducting sphere positive as illustrated in figure 1(b). The spherical coil surface has been meshed with $T = 4240$ elements and $N = 2122$ nodes. Henceforth in this paper, we shall refer to CoilS0 and CoilS to the solutions of equation 12 and equation 14 for the spherical geometry case, respectively.

4.3. Hemispherical coils

Open geometries, such as spherical-shaped cap or hemispherical forms, have been also frequently suggested in the literature [10], [9], as they offer natural aperture for patient access. In order to study the click sound reduction in open geometries, here we propose to investigate the design of a minimum stored-energy TMS coil with hemispherical shape with a radius of 9 cm, which must generate a maximized E-field in a prescribed spherical region of interest (ROI) of radius 1 cm, made up of $M = 400$ points and that is shifted by 5 cm in the positive $z-$direction from the centre of the base of the conducting hemisphere, as shown in figure 1(c).
The reference TMS stimulator for this geometry is referred to as CoilH0, and it is obtained through the solution of equation 12, whereas CoilH is the corresponding minimum Lorentz self-force hemispherical coil solution of equation 14.

4.4. Forward Problem

The solution of each optimisation problem allows the identification of the optimal nodal values of the stream function, whereas the wire arrangement that approximates the continuous current distribution is found by contouring the stream function [8].
In this work, the value of each coil inductance is evaluated by using FastHenry © [17], and assuming the coil wires have a 1.5 mm radius. Moreover,

sinusoidal variation ($f = 2.5$kHz) of the coil current with peak value of 5 kA has been considered for all cases.
Forward calculations of the Lorentz self-forces and the magnetic field produced by each TMS coil have been found by employing the elemental Biot-Savart expression applied directly to the wire-paths. The induced E-field of each TMS coil solution has been acquired using an existing direct BEM [14]. Moreover depth and focality metrics as defined in [2] were employed to describe the spatial characteristics of the stimulation.

In order to study acoustic behaviour, FE models of the designed TMS coils were created, where the elastic deformation of the TMS coils is calculated using the linear static solver provided by the commercial software MSC/NASTRAN. Each FE model is made up of one layer of quadrangular or triangular shell elements with 4 mm thickness that simulate the copper windings, where the coil deflection is computed by applying the previously found Lorentz self-force distribution to the nodes of the FE model.

5. Results

Results for the TMS coil design problems presented in section 4 are illustrated briefly in the following.

5.1. Rectangular Flat Coils

The wire paths solution for CoilP0 and CoilP design problems are depicted in figures 2(a)-2(b) respectively. As it can be appreciated, both rectangular TMS coils are formed by two lobes of wire (red paths indicate reversed current flow with respect to blue), where the winding density of CoilP is less concentrated over the region of stimulation than its counterpart CoilP0. This change in the wire distribution affects slightly the performance of CoilP compared to CoilP0, as can be seen in Table 1.
The magnetic field is distributed differently at the surface of CoilP0 compared to CoilP, as can it be appreciated in figures 3(a) and 3(b) respectively, where the maximum value of magnetic flux density calculated is similar for both TMS stimulator, more precisely, 2.06 T and 2.01 T for CoilP0 and CoilP, respectively.
The Lorentz self-force density distributions developed in the coil windings of CoilP0 and CoilP are depicted in figures 4(a) and 4(b) respectively. In both cases, the calculated forces act radially in the coil plane, causing an expansion of the wires, where in this case, the maximum magnitude of Lorentz force

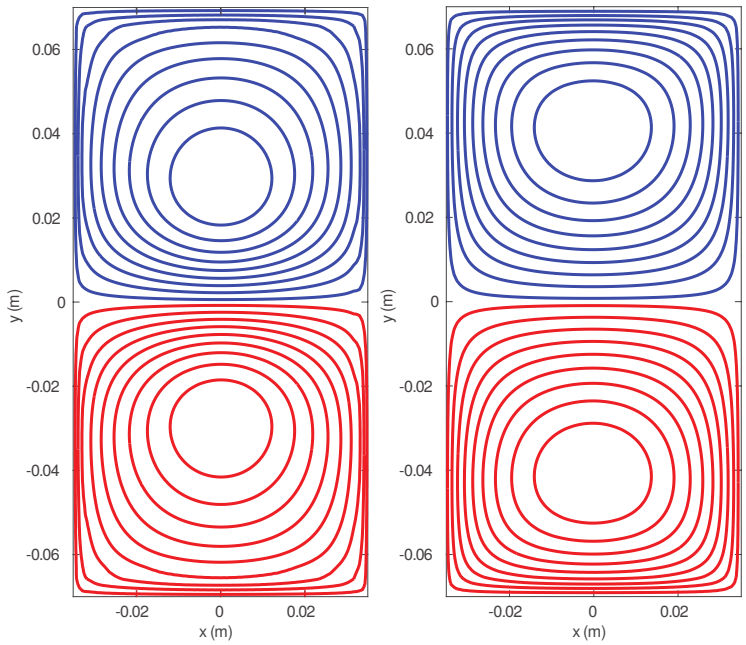

Figure 2: *Wire arrangements with 18 turns of (a) CoilP0 and (b) CoilP. Red wires indicate reversed current flow with respect to blue.*

densities found were 8.02 $\times 10^8$ N·m^{-3} and 7.99 $\times 10^9$ N·m^{-3} for CoilP0 and CoilP, respectively.

The deflection shape in response to the experienced Lorentz self-forces is displayed in figures 3(a) and 3(b) for CoilP0 and CoilP respectively, where displacements have been magnified up to a 10% of the characteristic coil length for ease of viewing. A constraint condition was added to the FE model for rectangular flat coils studies to simulate the real conditions, all nodes along a 45 mm centred line on the long right side were fixed.

In both cases, the greatest deflections clearly occur at the left corners of the conducting surface, in the opposite side where the constraint condition was considered, as a result of which the coil undergoes a significant expansion displacement in the left side.

Furthermore, in order to get more insight in the mechanical stability calculations of the von Mises stress have been performed, where the highest stress values found were 3.34 MPa and 3.14 MPa for CoilP0 and CoilP, respectively.

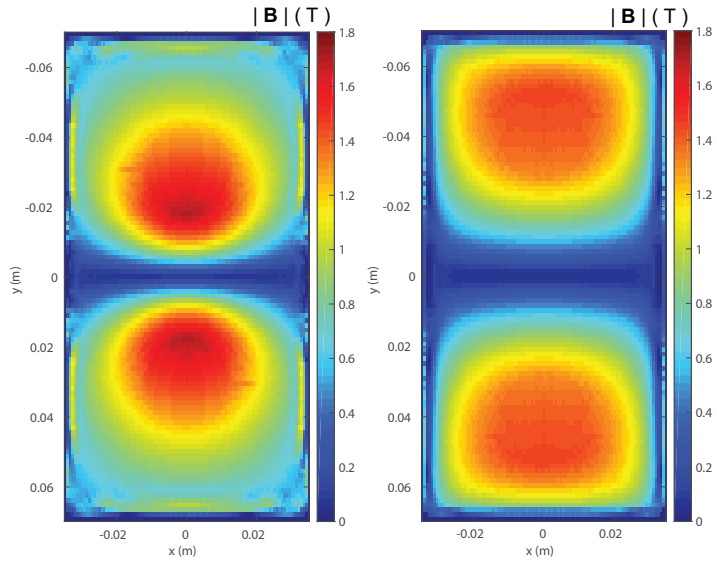

(a) (b)

Figure 3: *Calculated values of the magnetic field modulus at the plane of a) CoilP0 and b) CoilP.*

5.2. Spherical coils

The winding pattern solutions to CoilS0 and CoilS optimization problems are shown in figures 6(a) and 6(b) respectively, where it can be appreciated that there is a higher density of winding turns over the region of stimulation in both cases.

The two spherical TMS coils develop similar performances and produce stimulations with comparable spatial characteristics, as it can be seen in Table 1.

The magnetic fields at the surface of both spherical stimulators present a similar pattern, as it is shown in figures 7(a) and 7(b), nonetheless the maximum value of the magnetic flux modulus for the optimized design CoilS is lower than the corresponding one calculated for CoilS0, as it can be seen in Table 1.

The Lorentz self-force distributions developed in windings of CoilS0 and CoilS are schematically depicted in figures 7(c) and 7(d) respectively. For both TMS coils, the calculated forces produce an expansion of each lobe of wires, where the maximum value of the computed self-force densities are 4.30×10^8

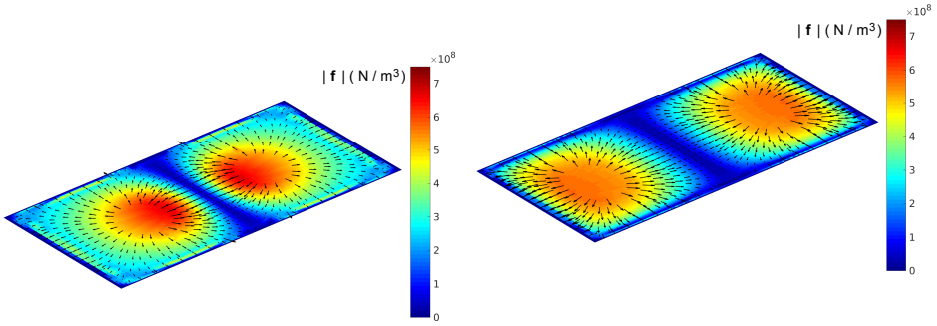

(a) (b)

Figure 4: *Lorentz self-force density experienced by a) CoilP0 and b) CoilP.*

$\mathrm{N{\cdot}m^{-3}}$ and 2.79 $\times 10^8$ $\mathrm{N{\cdot}m^{-3}}$, for CoilS0 and CoilS respectively.
The mechanical response of the spherical coils can be evaluated in figures 8(a) and 8(b), where the deflections experienced by CoilS0 and CoilS are illustrated respectively. The calculated displacements are again magnified up to a 10% of the characteristic coil length for ease of viewing.
A constraint condition was added to the FE model to simulate the real installation conditions; more precisely, the spherical coils were constrained by imposing clamping conditions in four nodes in the lower part of the sphere, depicting the support situation shown in 8(a) and 8(b).
In both cases, the greatest deflections occur at the top side of the sphere, producing an expansion displacement. The highest stresses calculated are 1.09 $\times 10^7$ Pa and 0.94 $\times 10^7$ Pa for CoilS0 and CoilS respectively.

5.3. Hemispherical coils

Figures 9(a) and 9(b) show the obtained winding pattern for coil design problems CoilH0 and CoilH respectively, whereas the corresponding parameters of these two hemispherical TMS coils are listed in Table 1, demonstrating a comparable performance of both coils.
The magnetic fields at the surface of both hemispherical stimulators follow a similar pattern, as it can be seen in figures 7(a) and 7(b), where maximum value of the magnetic flux found is of $|\mathbf{B}_{max}| = 1.12$ T for CoilH, and $|\mathbf{B}_{max}| = 1.26$ T for CoilH0.
Figures10(c) and 10(d) illustrate the Lorentz self-forces computed for CoilH0 and CoilH respectively. The forces produce again an expansion of the wires,

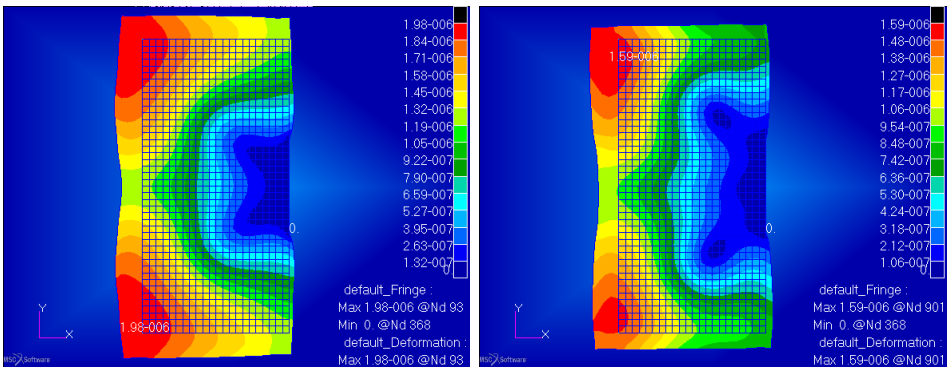

(a) (b)

Figure 5: *The deflection shape in response to Lorentz forces of a) CoilP0 and b) CoilP. Displacements have been up to a* 10% *of the characteristic coil length for ease of visualization.*

with a maximum magnitude of 1.26 $\times 10^9$ N·m^{-3} for the reference CoilH0, and 1.12 $\times 10^9$ N·m^{-3} for CoilH.

The acoustic response of the hemispherical stimulators has been computed by considering a constraint condition in the FE model to simulate the real installation condition, the TMS coils were restrained by clamping the nodes along the equator.

The deflection caused to CoilH0 and CoilH by the Lorentz self-force is shown in Figures11(a) and 11(b), respectively, where again, for ease of visibility, the deflections have been magnified up to a 10% of the characteristic coil length for ease of viewing. Although smaller deflections are found in other surface regions, the greatest deflections occur at the pole of the hemisphere, generating a similar main displacement of the top of both coils in the direction of the positive z-axis.

Analysis of the mechanical stability has been also developed for hemispherical TMS coils, and the highest von Mises stresses found are 1.72 MPa and 1.64 MPa for CoilH0 and CoilH respectively.

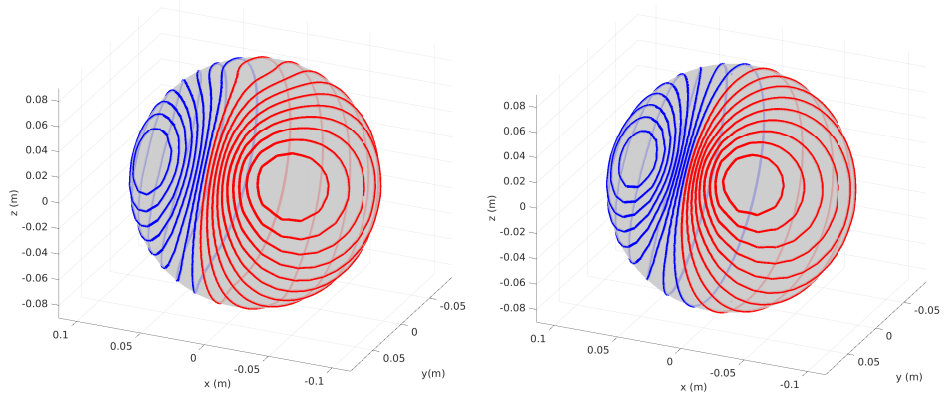

(a) (b)

Figure 6: *Wire arrangements with 18 turns of (a) CoilS0 and (b) CoilS. Red wires indicate reversed current flow with respect to blue.*

	L (μH)	R ($m\Omega$)	$D_{1/2}$ (cm)	$S_{1/2}$ (cm^2)	Contour levels	$\lvert\mathbf{B}_{max}\rvert$ (T)	$\lvert\mathbf{f}_{max}\rvert$ (N·m^{-3})	σ_{max} (MPa)
CoilP0	9.7	69	1.17	6.0	18	2.06	8.02 $\times 10^8$	3.34
CoilP	11.2	75	1.39	6.1	18	2.01	7.99 $\times 10^8$	3.14
CoilS0	18.1	134	2.01	20.3	18	1.08	4.30 $\times 10^8$	1.09
CoilS	19.0	152	2.15	22.2	18	0.91	2.79 $\times 10^8$	0.94
CoilH0	12.4	104	2.20	24.3	18	1.26	4.64 $\times 10^8$	1.72
CoilH	14.6	118	2.23	26.7	18	1.12	4.43 $\times 10^8$	1.64

Table 1: *TMS coil performance parameters:* L *is the inductance,* R *the resistance, $S_{1/2}$ the effective surface area (focality), $D_{1/2}$ the penetration or depth, the number of levels in which the stream function is contoured to produce the wire paths, $|\boldsymbol{B}_{max}|$ maximum magnetic field at the coil surface, $|\boldsymbol{f}_{max}|$ maximum Lorentz self-force at the coil surface and σ_{max} maximum stress. Simulated values of L and R were obtained using FastHenry © [17] using 3 mm diameter circular cross-section wire.*

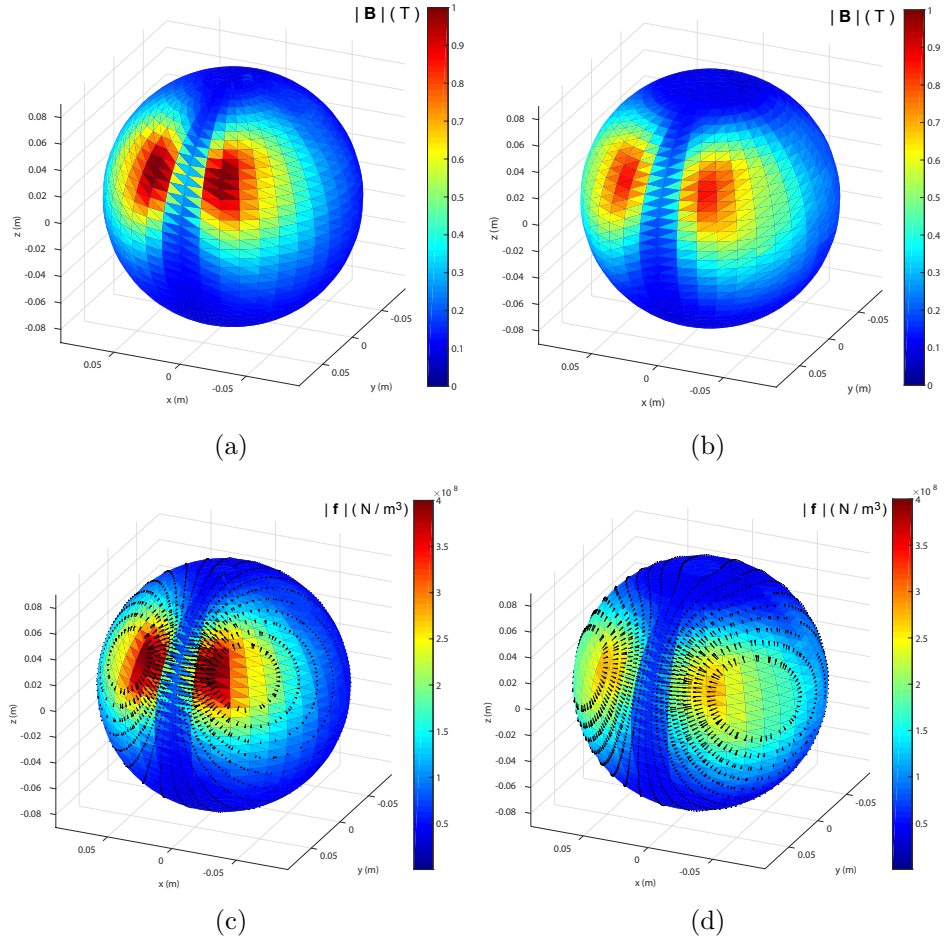

Figure 7: *Calculated values of the magnetic field modulus at the surface of a) CoilS0 and b) CoilS. Lorentz self-force density experienced by c) CoilS0 and d) CoilS.*

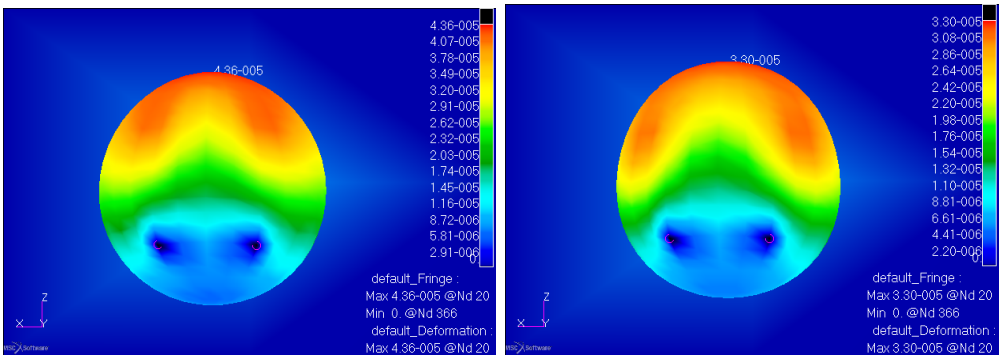

(a) (b)

Figure 8: *The deflection shape in response to Lorentz forces of a) CoilS0 and b) CoilS. Displacements have been magnified up to a* 10% *of the characteristic coil length for ease of visualization.*

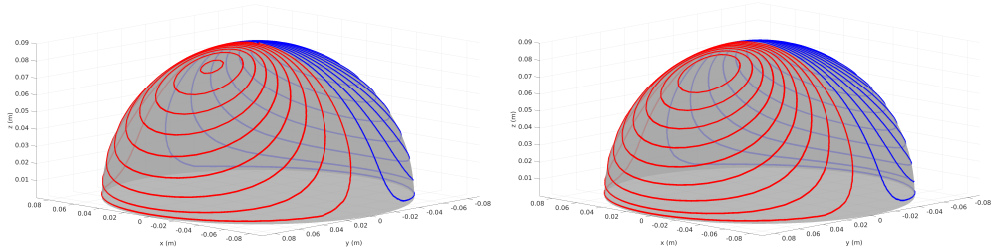

(a) (b)

Figure 9: *Wire arrangements with 18 turns of (a) CoilH0 and (b) CoilH. Red wires indicate reversed current flow with respect to blue.*

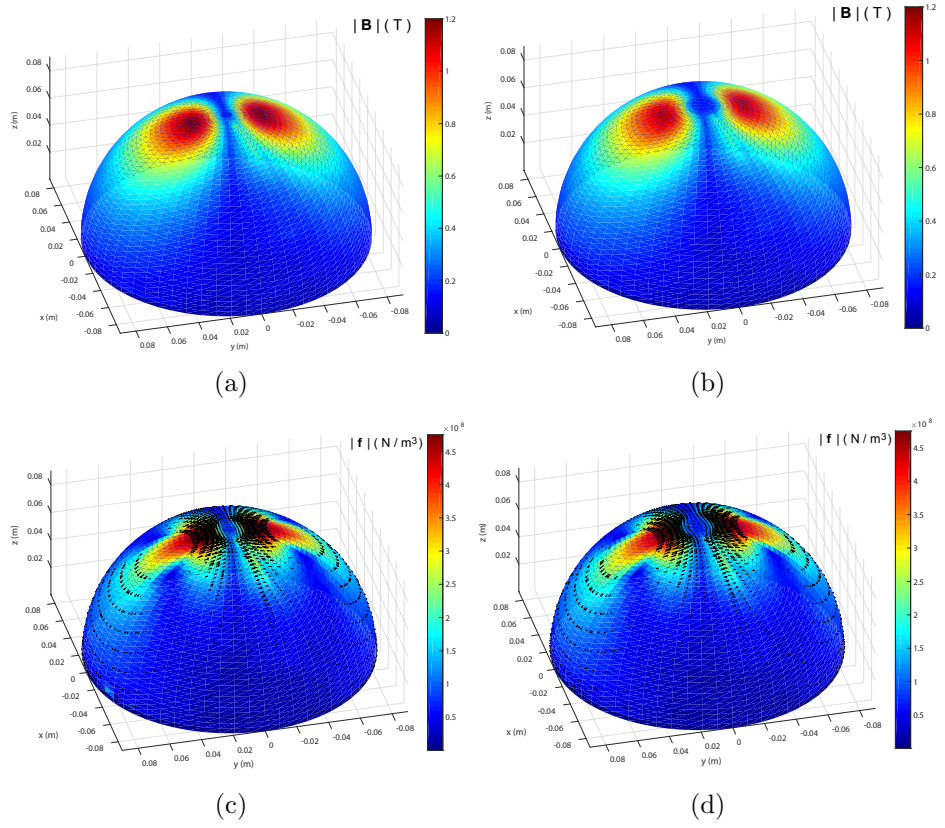

Figure 10: *Calculated values of the magnetic field modulus at the surface of a) CoilH0 and b) CoilH. Lorentz self-force density experienced by c) CoilH0 and d) CoilH.*

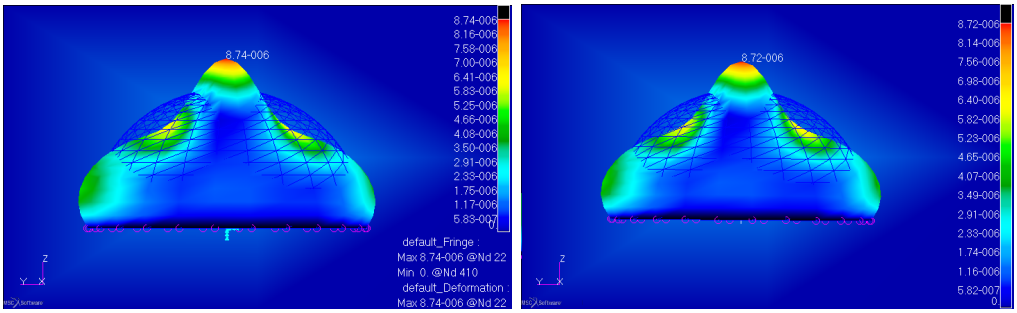

(a) (b)

Figure 11: *The deflection shape in response to Lorentz forces of a) CoilH0 and b) CoilH. Displacements have been magnified up to a* 10% *of the characteristic coil length for ease of visualization.*

6. Discussion

This paper reports a IBEM approach to reduce the acoustic noise in TMS coils by minimizing the Lorentz self-force. It has been applied to design coils of different geometries, which have been chosen for demonstration purposes as they are frequently used in the literature. So it is worth stressing that the design methodology performs well for many other different surfaces.

In order to guarantee the optimality of the produced TMS coils, they have been designed by incorporating a novel formulation of the Lorentz self-force into a convex optimization problem, which has been solved by extending a supporting vector framework developed by the authors [16].
In the proposed optimization scheme, the calculation of the matrix C, equation 14, implies a considerable computational burden, especially when using fine meshes. This can be significantly reduced by considering $\mathcal{F}_{j,t}$ matrices as sparse ones.

For all geometries tackled here, the TMS coils produced with this technique present reduced Lorentz self-force distributions compared to the reference stimulators. This decrease is of approximately of 14% for flat rectangular and spherical shapes, and of 5% for the hemispherical form. This reduction in the Lorentz self-force results into an improved acoustic response of the optimized coils (CoilP, CoilS, and CoilH) in contrast to the conventional ones (CoilP0, CoilS0, and CoilH0), as the reduction in the largest deformation is of 20%, 24% and 2% for flat rectangular, spherical and hemispherical forms, respectively.

In general, the improvement in the mechanical response slightly degrades the coil performance, as CoilP, CoilS, and CoilH present higher inductance and focality (see Table 1) than their conventional counterparts, point that illustrates a trade-off between competing requirements.
In fact, intermediate solutions between optimized and reference coils can be achieved for each geometry. If ψ_0 denotes the solution of equation 12, the following TMS coils design optimization problem can be also posed

$$\begin{cases} \max \|\mathcal{E}_x\psi\|_2^2 + \|\mathcal{E}_y\psi\|_2^2 + \|\mathcal{E}_z\psi\|_2^2 \\ \min \psi^T L\psi \\ \text{subject to } \|C\psi\|_2^2 < \alpha \|C\psi_0\|_2^2, \end{cases} \tag{15}$$

where $\alpha \in [0, 1]$ is a parameter that defines the extent by which the Lorentz self-force can be reduced with respect the reference coil.

Furthermore, in the study of the mechanical stability of the designed TMS devices, calculation of the von Mises stress was performed, and it was found that the coils with minimum Lorentz self-force show less fatigue than the corresponding conventional stimulator for all the studied geometries, being the maximum stress below the yield strength of copper (70 MPa) for all TMS coils.

In the mechanical analysis of the TMS coils, suitable constraint conditions must be included into the FE model to reproduce realistic conditions. Simulations have been carried out with the constraints shown in this work and other practical choices, and as expected, the acoustic response of the stimulators depends strongly on the type restriction considered. For instance, the low reduction in the calculated deflection of CoilH compared to that one found for CoilH0 is related to the restrictive constraint conditions imposed by clamping all nodes along the equator. Nonetheless, it is worth highlighting that the TMS coils designed with the proposed method show significant acoustic noise reduction compared to the reference devices in most of the studied constraint conditions.
It also worth noting that, the use of FE linear static analysis is justified, as in all studied cases the first natural frequency is greater than the force frequency (2.5 kHz).

Moreover, the presented IBEM approach can be combined with other noise reduction strategies, such as, control of the current pulse shape (to reduce the audible frequencies components) or implementation of coil structures with dedicated layers (for acoustic decoupling and dissipation) [5]-[6] to produce a general framework to produce effective quiet TMS.

7. Conclusions

The loud click noise produced by TMS devices is a significant obstacle in the progress of this medical technique and its application in cognitive neuroscience, as it affects brain activity degrading TMS precision, and makes TMS less safe and more obnoxious.
The acoustic source in TMS is found in the coil winding vibrations due to the Lorentz self-forces between the currents in the coil and the magnetic field they produce.

In this work, a stream function IBEM has been presented for designing coils with minimum Lorentz self-forces as an approach to produce TMS

devices with lower acoustic emission. Computational models have been adequately formulated to be incorporated into an optimization framework, which has been specifically developed to be solved using supporting vector analysis. Several examples of TMS coils of different geometries have been designed with the proposed technique, and the obtained results demonstrate that would have substantially lower Lorentz self-forces compared to conventional TMS. In order to study the acoustic response of the proposed TMS stimulators, the deflections resulting from Lorentz self-forces were evaluating by using commercial software MSC/NASTRAN, in which FE models of the coils were created and simulated. Although the vibration response of the TMS coils depends notably on the constraint conditions imposed in the FE model, it has been found that the TMS stimulators designed with the proposed method exhibit a reduction of the coil deflection (and son improved acoustic behaviour) compared to the reference devices in all studied conditions.
In this sense, the presented technique can be used as a valuable tool in the prediction of the vibration and acoustic noise generated by a TMS coil in the design stage.

In a future model, we aim to consider a even more realistic models of the TMS coil system to fully understand the vibration modes, resonances or noise transmission characteristics. Nevertheless, this work has demonstrated that the effects of optimizing the Lorentz self-forces is an effective strategy to achieve quieter TMS device, which can be combined with the existing technical solutions to satisfy the important need of reducing acoustic emission in TMS.

Acknowledgements

This work was supported by Junta de Andalucia under Marco del programa Operativo Feder Andalucia 2014- 2020.

[1] Wassermann E M, Epstein C M, Ziemann U, Walsh V, Paus T, Lisanby S H, editors 2008 . The Oxford handbook of transcranial magnetic stimulation. New York: Oxford University Press;

[2] Deng Z D, Lisanby S H and Peterchev A V 2013. Electric field depth-focality tradeoff in transcranial magnetic stimulation: simulation comparison of 50 coil designs. *Brain Stimul* 6:1-13

[3] Rossi S, Hallett M, Rossini PM, Pascual-Leone A 2009, Safety of TMS Consensus Group. Safety, ethical considerations, and application guidelines for the use of transcranial magnetic stimulation in clinical practice and research. Clin Neurophysiol. 2009;120:200839.

[4] Bungert A 2010, *TMS combined with fMRI*, PhD Thesis, University of Nottingham, 2010.

[5] Goetz SM, Murphy DL, Peterchev AV 2014. Transcranial magnetic stimulation device with reduced acoustic noise. *IEEE Mag Lett* 2014;5:1500104.

[6] Peterchev AV, Murphy DLK and Goetz SM, Quiet transcranial magnetic stimulation: Status and future directions, *37th Annual International Conference of the IEEE Engineering in Medicine and Biology Society* (EMBC), Milan, 2015, pp. 226-229.

[7] Koponen L M, Nieminen J O, Ilmoniemi R J 2014. Minimum-energy coils for transcranial magnetic stimulation: application to focal stimulation. *Brain Stimul.* ;8(1):124-34.

[8] Cobos Sanchez C , Guerrero Rodriguez J M, Quiros Olazabal A and Blanco-Navarro D 2017a, Novel TMS coils designed using an inverse boundary element method, *Physics in Medicine and Biology*, Volume 62, Pages 73-90.

[9] Cobos Sanchez C, Garcia-Pacheco F, Guerrero Rodriguez J M, Hill R 2018, An inverse boundary element method computational framework for designing optimal TMS coils. *Engineering Analysis with Boundary Elements*, **88**, 156-169.

[10] Gomez L J, Goetz SM, Peterchev AV 2018, Design of transcranial magnetic stimulation coils with optimal trade-off between depth, focality, and energy, *Journal of Neural Engineering*. 15 046-033

[11] B Wang, Sheen MR, Deng Z D, Smith JE, Tharayil JJ, Gurrey CJ, Gomez LJ, Peterchev AV 2018, Redesigning existing transcranial magnetic stimulation coils to reduce energy: application to low field magnetic stimulation, *Journal of Neural Engineering*, 15,3, 036022

[12] Forbes L K, Brideson M A, Crozier S and While P T 2007, Calculating the movement of MRI coils, and minimizing their noise, ANZIAM J. vol. 49, 17-35.

[13] Crowther L J, Porzig K, Hadimani R L, Brauer H and Jiles C 2013, Realistically Modeled Transcranial Magnetic Stimulation Coils for Lorentz Force and Stress Calculations During MRI, *IEEE Transactions on Magnetics*, vol. 49, no. 7, pp. 3426-3429, July 2013.

[14] Cobos Sanchez C, Bowtell R, Power H, Glover P, Marin L, Becker A and Jones A 2009 Forward electric field calculation using BEM for time-varying magnetic field gradients and motion in strong static fields *Eng. Anal. Bound. Elem.* 33 1074-88

[15] Cobos Sanchez C, Gonzalez Garcia S and Power H 2010a E-coil: an inverse boundary element method for a quasi-static problem, *Physics in Medicine and Biology*, vol. 55, 3087−3100.

[16] Cobos Sanchez C, Garcia-Pacheco, Moreno-Pulido S, Saez-Martinez S 2017b, Supporting vectors of continuous linear operators, *Ann Funct Anal.* **8** (2017), no. 4, 520–530.

[17] Kamon M Tsuk M J and White J K 1994 FASTHENRY: A Multipole-Accelerated 3-D Inductance Extraction Program *IEEE Transactions on Microwave Theory and Techniques* **42** 1750−1758

Appendix A: Boundary integral equation formulation

Equation 1 introduces the current density at each element, which can be written in terms of the nodal values of the stream function and elements of the local geometry equation. This current density model can be used to produce the discretized expressions for the following physical magnitudes involved in the design problem.

Magnetic vector potential

The magnetic vector potential, $\mathbf{A}$, can be determined from

$$\mathbf{A}(\mathbf{r}) = \frac{\mu_0}{4\pi} \int_S \frac{\mathbf{J}(\mathbf{r}')}{|\mathbf{r} - \mathbf{r}'|} \, dS \tag{.1}$$

and by applying equation 1, this yields

$$\mathbf{A}(\mathbf{r}) = \frac{\mu_0}{4\pi} \sum_{n=1}^{N} \psi_n \int_S \frac{\boldsymbol{\jmath}^n(\mathbf{r}')}{|\mathbf{r} - \mathbf{r}'|} \, dS \tag{.2}$$

and if the conducting surface is approximated by the union of the T elements

$$\mathbf{A}(\mathbf{r}) = \frac{\mu_0}{4\pi} \sum_{n=1}^{N} \psi_n \sum_{t=1}^{T} \int_{S_t} \frac{\boldsymbol{\jmath}^n(\mathbf{r}')}{|\mathbf{r} - \mathbf{r}'|} \, dS'. \tag{.3}$$

To simplify the notation we can write $\mathbf{A}$ as a linear combination of the magnetic potentials produced by the current element associated with each node.

$$\mathbf{A}(\mathbf{r}) = \sum_{n=1}^{N} \psi_n \mathbf{a}^n(\mathbf{r}), \tag{.4}$$

where $\mathbf{a}^n(\mathbf{r})$ is the magnetic potential produced by a unit stream function at the nth-node.

Magnetic Induction

If we apply the curl operator to equation .4, an expression for the magnetic induction produced by the current coil is then obtained

$$\mathbf{B}(\mathbf{r}) = \sum_{n=1}^{N} \psi_n \mathbf{b}^n(\mathbf{r}), \tag{.5}$$

where $\mathbf{b}^n(\mathbf{r})$ is the magnetic induction (equivalently magnetic field) produced by a unit stream function at the nth-node, that is

$$\mathbf{b}^n(\mathbf{r}) = \frac{\mu_0}{4\pi} \sum_{t=1}^{T} \int_{S_t} \nabla \times \frac{\boldsymbol{\jmath}^n(\mathbf{r}')}{|\mathbf{r} - \mathbf{r}'|} \, dS'. \tag{.6}$$

Stored magnetic Energy

Operating in a similar fashion the stored magnetic energy in the TMS coil can be written as

$$W = \frac{\mu_0}{8\pi} \int_S \int_{S'} \frac{\mathbf{J}(\mathbf{r})\mathbf{J}(\mathbf{r}')}{|\mathbf{r} - \mathbf{r}'|} dS dS' = \frac{1}{2} \sum_{n=1}^{N} \sum_{m=1}^{N} \psi_n \psi_m L_{mn} \tag{.7}$$

where L_{mn} is the mutual inductance between the m^{th} and n^{th} current elements

$$L_{mn} = \frac{\mu_0}{4\pi} \int_S \int_{S'} \frac{\boldsymbol{\jmath}^n(\mathbf{r}) \cdot \boldsymbol{\jmath}^m(\mathbf{r}')}{|\mathbf{r} - \mathbf{r}'|} \, dS dS'. \tag{.8}$$

Electric field

To produce a formulation for the electric field, we recall that there are two sources of $\mathbf{E}$, the first is the temporal derivative of the vector potential, $\mathbf{A}$, and it is produced by current flowing in the coils; the change of $\mathbf{A}$ produces initially a redistribution of free charges in the conducting domain, which accumulate at boundaries between regions of different conductivity and generate the second, conservative contribution to $\mathbf{E}$

$$\mathbf{E} = -\nabla\phi - \frac{\partial \mathbf{A}}{\partial t}. \tag{.9}$$

The characterization of the magnetic component can be found in section 7 of the Appendix A; whereas the integral representation of conservative component of the E-field can be produced if we recall the harmonic nature of the scalar potential. Thus if a multi-compartment volume conductor D (where the ROI is included) is made of M different homogeneous sub-domains, D_i ($D = \bigcup_i^M D_i$), in each of theses subregions with uniform conductivity the scalar potential satisfies Laplace's equation.
Moreover, if we use the continuity of the current flowing at every surface between regions as a boundary condition (which is a natural or Neumann condition since the normal derivative of the potential is specified) the conservative

part of the electric field at a point of the ROI2 inside the pth sub-domain system can be written as [14]

$$\frac{\partial \phi}{\partial x_j}(\mathbf{r}) = \sum_{i=0}^{M} \frac{(\sigma_i - \sigma_{i+1})}{\sigma_p} \int_{S_i} \Big[- \frac{\partial \phi^*}{\partial x_j}(\mathbf{r}, \mathbf{y}) \frac{\partial A^n}{\partial t}(\mathbf{y}) - \frac{\partial q^*}{\partial x_j}(\mathbf{r}, \mathbf{y})\ \phi^i(\mathbf{y}) \Big] ds(\mathbf{y}), \qquad \mathbf{r} \in D_p, \qquad p = 1, ..., M. \tag{.10}$$

where $\sigma_i,\ i = 1, ..., M$, is the conductivity of each subdomain, the Green's function dipole is given by

$$\frac{\partial \phi^*}{\partial x_j} = - \frac{x_j - y_j}{4\pi r^3}, \qquad j = 1, 2, 3, \tag{.11}$$

and the quadrupole and is

$$\frac{\partial q^*}{\partial x_j} = - \frac{1}{4\pi} \Big[\frac{\delta_{j,k}}{r^3} - 3 \frac{(x_j - y_j)(x_k - y_k)}{r^5} \Big] n_k, \qquad j = 1, 2, 3. \tag{.12}$$

Here, we have used the tensor summation definition of the double index.

Appendix B: Optimization

A multiobjective optimization problem of the form

$$\begin{cases} \max f_i(x) & i = 1, \ldots, n \\ \min g_j(x) & j = 1, \ldots, m \end{cases}$$

might not have a solution, that is, there might not exist an x_0 such that $f_i(x_0) \geq f_i(x)$ and $g_j(x_0) \leq g_j(x)$ for all feasible x's, all $i = 1, \ldots, n$ and all $j = 1, \ldots, m$. If this is the case, then the multiobjective optimization problem needs to be reformulated, if possible, by reducing the number of objective functions, since the presence of many objective functions is what causes the lack of solutions.

Different reformulations may lead to different solutions, so then, which reformulation should we apply. First of all, it seems natural not to mix the functions to maximize with the functions to minimize. Also, our reformulation should be framed in the same mathematical scope as the original problem, that is, if the original problem is framed in certain spaces (the domain of the objective functions), then the reformulation should also be

framed in the same spaces. And finally, the reformulation should be applied in such a way that it must have a solution and it has to model accurately the real-life problem where the original optimization problem comes from.

In the particular case of this manuscript, the original multiobjective optimization problem that better models the real-life problem is the following:

$$\begin{cases} \max \|\mathcal{E}_x\psi\|_2^2 & \\ \max \|\mathcal{E}_y\psi\|_2^2 & \\ \max \|\mathcal{E}_z\psi\|_2^2 & \\ \min \psi^T\mathcal{F}_{ix}\psi & i=1,\ldots,T \\ \min \psi^T\mathcal{F}_{iy}\psi & i=1,\ldots,T \\ \min \psi^T\mathcal{F}_{iz}\psi & i=1,\ldots,T \\ \min \psi^T L\psi & \end{cases} \tag{.1}$$

where $\mathcal{E}_j, \mathcal{F}_{ij}, L \in \mathbb{R}^{n\times n}$ for $j = x, y, z$ and $i = 1, \ldots, T$. The following theorem assures that the multiobjective optimization problem (.1) has no solution.

Theorem 1. *No $\psi_0 \in \mathbb{R}^n$ verifies that*

$$\begin{cases} \|\mathcal{E}_x\psi_0\|_2^2 \geq \|\mathcal{E}_x\psi\|_2^2 & \forall\psi\in\mathbb{R}^n & \\ \|\mathcal{E}_y\psi_0\|_2^2 \geq \|\mathcal{E}_y\psi\|_2^2 & \forall\psi\in\mathbb{R}^n & \\ \|\mathcal{E}_z\psi_0\|_2^2 \geq \|\mathcal{E}_z\psi\|_2^2 & \forall\psi\in\mathbb{R}^n & \\ \psi_0^T\mathcal{F}_{ix}\psi_0 \leq \psi^T\mathcal{F}_{ix}\psi & \forall\psi\in\mathbb{R}^n & i=1,\ldots,T \\ \psi_0^T\mathcal{F}_{iy}\psi_0 \leq \psi^T\mathcal{F}_{iy}\psi & \forall\psi\in\mathbb{R}^n & i=1,\ldots,T \\ \psi_0^T\mathcal{F}_{iz}\psi_0 \leq \psi^T\mathcal{F}_{iz}\psi & \forall\psi\in\mathbb{R}^n & i=1,\ldots,T \\ \psi_0^T L\psi_0 \leq \psi^T L\psi & \forall\psi\in\mathbb{R}^n & \end{cases}$$

Proof: If such ψ_0 exists, then for instance

$$\|\mathcal{E}_x\psi_0\|_2^2 \geq \|\mathcal{E}_x(2\psi_0)\|_2^2 = 4\|\mathcal{E}_x\psi_0\|_2^2,$$

which is impossible unless $\psi_0 = 0$. Also,

$$\psi_0^T L\psi_0 \leq 0^T L0 = 0,$$

which again implies that $\psi_0 = 0$ due to the fact that L is positive-definite. Then it only suffices to take any $\psi_1 \in \mathbb{R}^n$ such that $\mathcal{E}_j(\psi_1) \neq 0$ for some $j \in \{x, y, z\}$. By assumption on ψ_0, it occurs that

$$0 = \|\mathcal{E}_j\psi_0\|_2 \geq \|\mathcal{E}_j\psi_1\|_2 > 0,$$

which is a contradiction. As a consequence, such ψ_0 cannot exist.

We will now apply some basic linear algebra techniques to rewrite the problem (.1). Notice that this is not a reformulation in the sense remarked at the beginning of this appendix. Observe that, for each $i \in \{1, \ldots, T\}$, $\mathcal{F}_{ix}$, $\mathcal{F}_{iy}$, $\mathcal{F}_{iz}$ and L are positive-definite so we can apply the Cholesky decomposition to them obtaining $L = C_0^T C_0$ and $\mathcal{F}_{ij} = C_{ij}^T C_{ij}$ for $i = 1, \ldots, T$ and $j = x, y, z$. Thus $\psi^T L \psi = \|C_0\psi\|_2^2$ and $\psi^T \mathcal{F}_{ij} \psi = \|C_{ij}\psi\|_2^2$ for $i = 1, \ldots, T$ and $j = x, y, z$. Now we obtain the multi-objective optimization problem:

$$\begin{cases} \max \|\mathcal{E}_j \psi\|_2^2 & j = x, y, z \\ \min \|C_{ij}\psi\|_2^2 & i = 1, \ldots, T \quad j = x, y, z \\ \min \|C_0\psi\|_2^2 \end{cases} \tag{.2}$$

The problem (.2) is exactly the same problem as (.1) and thus it has no solution either. In other words, we can state the following theorem whose proof we omit since it is basically the same proof as that of Theorem 1.

Theorem 2. *No $\psi_0 \in \mathbb{R}^n$ verifies that*

$$\begin{cases} \|\mathcal{E}_j\psi_0\|_2^2 \geq \|\mathcal{E}_j\psi\|_2^2 & \forall \psi \in \mathbb{R}^n & j = x, y, z \\ \|C_{ij}\psi_0\|_2^2 \leq \|C_{ij}\psi\|_2^2 & \forall \psi \in \mathbb{R}^n & i = 1, \ldots, T & j = x, y, z \\ \|C_0\psi_0\|_2^2 \leq \|C_0\psi\|_2^2 & \forall \psi \in \mathbb{R}^n \end{cases}$$

The previous multi-objective optimization problem (.2) must be reformulated. Like we mentioned above, since we have to gather separately the objective functions to maximize and the objective functions to minimize, we will reformulate it to a problem of the form

$$\begin{cases} \max \|E\psi\|_2^2 \\ \min \|C\psi\|_2^2 \end{cases}$$

where E and C are matrices appropriately chosen. The choice of these two matrices is conditioned by the fact that here $\mathbb{R}^n$ is endowed with the $\|\cdot\|_2$-norm, that is, the Euclidean norm, which turns $\mathbb{R}^n$ into a Hilbert space $\ell_2^n := (\mathbb{R}^n, \|\cdot\|_2)$. Therefore, we must keep our problem framed in the Hilbert space setting. This leaves the only possibility that E and C have the following form:

$$\begin{array}{rccl} E: & \mathbb{R}^n & \to & \ell_2^3(\mathbb{R}^n) = \mathbb{R}^n \oplus_2 \mathbb{R}^n \oplus_2 \mathbb{R}^n = \ell_2^{3n} \\ & \psi & \mapsto & E\psi := (\mathcal{E}_x\psi, \mathcal{E}_y\psi, \mathcal{E}_z\psi) \end{array}$$

and

$$\begin{array}{rccl} C: & \mathbb{R}^n & \to & \ell_2^{1+3T}(\mathbb{R}^n) = \mathbb{R}^n \oplus_2 \cdots \oplus_2 \mathbb{R}^n = \ell_2^{n+3nT} \\ & \psi & \mapsto & C\psi := (C_0\psi, C_{1x}\psi, \ldots, C_{Tx}\psi, C_{1y}\psi, \ldots, C_{Ty}\psi, C_{1z}\psi, \ldots, C_{Tz}\psi). \end{array}$$

Notice that both ℓ_2^{3n} and ℓ_2^{n+3nT} are Hilbert spaces. We obtain then the following reformulation:

$$\left\{ \begin{array}{l} \max \|E\psi\|_2^2 = \|\mathcal{E}_x\psi\|_2^2 + \|\mathcal{E}_y\psi\|_2^2 + \|\mathcal{E}_z\psi\|_2^2 \\ \min \|C\psi\|_2^2 = \|C_0\psi\|_2^2 + \displaystyle\sum_{i=1}^{T} \sum_{j=x,y,z} \|C_{ij}\psi\|_2^2 \end{array} \right. \tag{.3}$$

where the matrices E and C are given by

$$E = \begin{pmatrix} \mathcal{E}_x \\ \mathcal{E}_y \\ \mathcal{E}_z \end{pmatrix}$$

and

$$C = \begin{pmatrix} C_0 \\ C_{1x} \\ \vdots \\ C_{Tx} \\ C_{1y} \\ \vdots \\ C_{Ty} \\ C_{1z} \\ \vdots \\ C_{Tz} \end{pmatrix}.$$

In (.3) we can obviously remove the squares from $\|E\psi\|_2^2$ and $\|C\psi\|_2^2$ obtaining

$$\left\{ \begin{array}{l} \max \|E\psi\|_2 \\ \min \|C\psi\|_2 \end{array} \right. \tag{.4}$$

Due to the absolute homogeneous character of the norm, that is, $\|\lambda\psi\|_2 = |\lambda|\|\psi\|_2$ for all $\lambda \in \mathbb{R}$ and all $\psi \in \mathbb{R}^n$, we are entitled to transform the objective function to minimize into a constraint. We then get:

$$\begin{cases} \max \|E\psi\|_2 \\ \|C\psi\|_2 \leq 1 \end{cases} \tag{.5}$$

Since C_0 is invertible, we can easily conclude, by means of basic linear algebra techniques, that $\ker(C) = \{0\}$. This fact has two consequences:

1. The set $\{\psi \in \mathbb{R}^n : \|C\psi\|_2 \leq 1\}$ is compact and thus problem (.5) has a solution.
2. C is left-invertible.

The appropriate left-inverse of C to choose is the Moore-Penrose inverse. Therefore, if C^+ denotes the Moore-Penrose inverse of C, then (.5) is equivalent to solving

$$\begin{cases} \max \|EC^+\phi\|_2 \\ \|\phi\|_2 \leq 1 \end{cases} \tag{.6}$$

Problem (.6) is a singular-value problem that can elegantly be solved by finding the supporting vectors of the matrix EC^+ for the $\|\cdot\|_2$-norm. We refer the reader to [16] for an elegant description of how to solve a singular-value problem by finding the supporting vectors for the Eculidean norm. Finally, if ϕ_0 is a supporting vector of EC^+, that is, a solution of (.6), and if we ask ϕ_0 to satisfy that $\operatorname{rank}(C) = \operatorname{rank}([C|\phi_0])$, then $\psi_0 := C^+\phi_0$ is a solution of (.5). Notice that the existence of a solution ϕ_0 of (.6) satisfying that $\operatorname{rank}(C) = \operatorname{rank}([C|\phi_0])$ is guaranteed by the compactness of the set

$$\{\psi \in \mathbb{R}^n : \|C\psi\|_2 \leq 1\}.$$

Since (.5) models the original real-life problem accurately due to the mathematical steps that we have followed, we conclude that ψ_0 is the appropriate solution we were looking for.